Catalysis Science & Technology

ROYAL SOCIETY OF CHEMISTRY

PAPER

View Article Online
View Journal | View Issue

Cite this: *Catal. Sci. Technol.*, 2023, 13, 2101

Ligand functionalization on Zr-MOFs enables efficient visible-light-driven H_2O_2 evolution in pure water†

Jianhao Qiu, Lu Zhang, Guanglu Xia, Dingliang Dai, Yong Tang and Jianfeng Yao *

Received 27th January 2023,
Accepted 15th February 2023

DOI: 10.1039/d3cy00130j

rsc.li/catalysis

Different ligand functionalized UiO-66 (UiO-66-X, X = OH, $(OH)_2$ and NH_2) were prepared and then modified by $ZnIn_2S_4$ lamellas to form $ZnIn_2S_4$/UiO-66-X heterostructures for visible-light-driven H_2O_2 evolution in pure water. The H_2O_2 yields using $ZnIn_2S_4$/UiO-66-NH_2, $ZnIn_2S_4$/UiO-66-$(OH)_2$ and $ZnIn_2S_4$/UiO-66-OH are 799, 733 and 165 μmol L^{-1}, respectively, which are 9.5, 8.7 and 2.0 times that of $ZnIn_2S_4$/UiO-66. The high performance of $ZnIn_2S_4$/UiO-66-NH_2 and $ZnIn_2S_4$/UiO-66-$(OH)_2$ is ascribed to the benign visible-light response and Z-scheme heterostructures, and the H_2O_2 evolution abides by indirect O_2 reduction with $^{\bullet}O_2^-$ as an intermediate species. Additionally, H_2O_2 yields using $ZnIn_2S_4$/UiO-66-NH_2 on tap water and Xuanwu Lake (Nanjing, China) water can be comparable to that on the above-deionized water. This study sheds light on the great promise of functionalized MOFs and their applications on green (photo)catalytic energy conversion.

1. Introduction

As an eco-friendly and versatile oxidant, hydrogen peroxide (H_2O_2) is of great significance in various areas, such as disinfection, pulp bleaching, organic synthesis and effluent treatment.[1,2] Additionally, on account of its high energy capacity, facile storage and transportation, H_2O_2 has been deemed as a promising and ideal liquid fuel.[3] Therefore, the market demand for H_2O_2 all over the world is pretty huge and will continuously increase. Currently, the main strategy to produce H_2O_2 in industry is the anthraquinone method, which undergoes consecutive hydrogenation and oxidation reactions, inducing large amounts of toxic byproduct generation and high energy input.[4] Within this context, photocatalytic evolution of H_2O_2 from O_2 reduction has drawn plenty of interest for the last few years.[5,6] In this respect, much effort on traditional semiconductors like CdS,[7] g-C_3N_4,[8] Bi_2MoO_6 (ref. 9) and $BiVO_4$ (ref. 3) as photocatalysts was devoted to H_2O_2 generation and indeed, their corresponding performances were admirable. Nonetheless, most of these reactions were performed in the presence of sacrificial agents (alcohols) and pure O_2, which makes the consequent separation of H_2O_2 difficult and requires extra energy input, consequently going against green-chemistry principles. Additionally, these photocatalysts normally have a low O_2 capture/adsorption capacity due to their limited surface areas.

Thanks to an inherent large surface area, high porosity, tailorable structure and semiconducting behavior,[10–12] metal–organic frameworks (MOFs) are vastly acclaimed in gas-associated photocatalysis, like photocatalytic CO_2 reduction[13] and N_2 fixation.[14] Whereas, MOFs utilized in H_2O_2 generation from O_2 photocatalytic reduction received only sporadic attention.[15] Yamashita and co-workers constructed hydrophobic MIL-125-NH_2 *via* ligand[16] or metal cluster[17] alkylation and achieved H_2O_2 production in a benzyl alcohol/water two-phase system, and later perylenetetracarboxylic diimide was grafted on MIL-125-NH_2 for H_2O_2 production in water.[5] Additionally, MOF/semiconductor hybrids like MIL-125-NH_2(TiO_2)/Ti_3C_2,[18] ZIF-8/g-C_3N_4 (ref. 19) and MIL-125-NH_2@ZnS (ref. 20) were also fabricated for H_2O_2 photocatalytic evolution.

Ligand decoration on MOFs, especially MOFs with terephthalic acid as ligands, could facilely and effectively regulate their physicochemical properties, conferring charming versatility.[10] The common route for ligand decoration is a substitution by functional groups, such as electron-donating amino and hydroxyl groups. The reasons are as follows: (1) uncoordinated hydroxyl and amino groups could serve as additional active sites to participate in the adsorption and activation of reactants,[21,22] and may also induce interactions with guest molecules when using MOFs as hosts to prepare adsorbents or catalysts;[23] (2) amino or

Jiangsu Co-Innovation Center of Efficient Processing and Utilization of Forest Resources, College of Chemical Engineering, Nanjing Forestry University, Nanjing 210037, China. E-mail: jfyao@njfu.edu.cn

† Electronic supplementary information (ESI) available. See DOI: https://doi.org/10.1039/d3cy00130j

hydroxyl substituents could serve as auxochromic and bathochromic groups in aromatic rings, rendering a redshift of light absorption;[24,25] (3) amino and hydroxyl groups are hydrophilic, which could promote the reaction in water. Given such a circumstance, it is believed that amino or hydroxyl-functionalized MOFs could possess great potential for photocatalytic H_2O_2 generation under visible light.

Considering the unprecedented thermal, chemical and mechanical stability, UiO-66, a zirconium-based MOF (each $Zr_6O_4(OH)_4$ cluster coordinates with 12 organic ligands),[26] was selected as the matrix. A series of UiO-66-X (X = OH, $(OH)_2$ and NH_2) was synthesized through a facile solvothermal method and then decorated by $ZnIn_2S_4$ layers for visible-light-driven H_2O_2 evolution in pure water and ambient air. $ZnIn_2S_4$ is a typical layered semiconductor with favorable chemical and photostability, enviable visible-light absorption and delicate band configuration with a strong reduction ability that can reduce O_2 into H_2O_2.[27,28] Thereby, $ZnIn_2S_4$ was adopted to sensitize UiO-66-X and constructed heterostructures to optimize the photocatalytic performances. On account of the favorable visible-light capture and unique Z-scheme heterostructures, $ZnIn_2S_4$ modified UiO-66-NH_2 and UiO-66-$(OH)_2$ performed remarkable activities for photocatalytic H_2O_2 evolution. This study would motivate the development of MOF functionalization in green photo- or electrocatalysis.

2. Experimental section

2.1 Materials

Zirconium chloride ($ZrCl_4$, 98%), 2-hydroxyterephthalic acid (≥98%) and 2,5-dihydroxyterephthalic acid (≥98%) were bought from Aladdin Industrial Company. *N*,*N*-Dimethylformamide (DMF), acetic acid, terephthalic acid (≥99%), ethanol, zinc acetate dihydrate (≥99%, $Zn(CH_3COO)_2{\cdot}2H_2O$) and thioacetamide (TAA, ≥99%) were obtained from Sinopharm Chemical Reagent. 2-Aminoterephthalic acid (99%) was purchased from Sigma-Aldrich. Indium chloride tetrahydrate ($InCl_3{\cdot}4H_2O$, ≥99%) was bought from Shanghai Macklin.

2.2 Preparation of functionalized Zr-MOFs

UiO-66-OH, UiO-66-$(OH)_2$ and UiO-66-NH_2 were prepared based on our previous report.[26] Typically for UiO-66-NH_2, 190.3 mg of $ZrCl_4$ (0.8 mmol), 147 mg of 2-aminoterephthalic acid (0.8 mmol) and 9.6 g of acetic acid (160 mmol) were added into 81.7 mL of DMF. After ultrasound treatment for 20 min and stirring for 2 h, the solution was transferred into a 150-mL autoclave and kept at 120 °C for 24 h. The products were collected by centrifugation, rinsed with DMF and methanol and finally dried at 80 °C overnight. UiO-66-OH, UiO-66-$(OH)_2$ and UiO-66 were prepared under the same conditions except that 2-aminoterephthalic acid was replaced by equimolar 2-hydroxyterephthalic acid, 2,5-dihydroxyterephthalic acid and terephthalic acid, respectively.

2.3 Zr-MOFs modified by $ZnIn_2S_4$ lamellas

In a typical synthesis, 169.3 mg of functionalized Zr-MOFs were dispersed in 15 mL of ethanol with ultrasound for 0.5 h. Meanwhile, 87.8 mg of $Zn(Ac)_2{\cdot}2H_2O$, 234.6 mg of $InCl_3{\cdot}4H_2O$ and 120.2 mg of TAA were dissolved into 15 mL of deionized water with stirring for 0.5 h. Subsequently, the above aqueous solution was dropped slowly into the ethanol suspension. After stirring for 2 h, the suspension was transferred into a 50 mL autoclave and kept at 180 °C for 24 h. The products were gathered by centrifugation, rinsed with water and ethanol and finally dried at 80 °C overnight. The obtained $ZnIn_2S_4$/Zr-MOFs samples (50 wt% of $ZnIn_2S_4$/Zr-MOFs) were named Z-UOH, Z-U$(OH)_2$ and Z-UN, respectively. As comparisons, $ZnIn_2S_4$/UiO-66 (Z-U) and bare $ZnIn_2S_4$ nanosheets were also prepared under the same conditions with UiO-66 and without any Zr-MOFs, respectively.

2.4 Characterizations

X-ray diffraction (XRD) patterns were obtained on a Rigaku Ultima IV instrument. N_2 adsorption–desorption isotherms were measured using a Micromeritics TriStar II equipment, and corresponding specific surface areas were determined by the Brunauer–Emmett–Teller (BET) method. Scanning electron microscopy (SEM) and energy dispersive X-ray spectrometry (EDS) mapping were carried out with a Hitachi Regulus 8100 instrument. Transmission electron microscopy (TEM) was performed using JEOL JEM-1400 and JEM-2100 instruments. UV-vis diffuse reflectance spectra (DRS) were recorded on a Shimadzu UV-2600 spectrophotometer. Fourier transform infrared spectroscopy (FTIR) was conducted on a Thermo Electron Nicolet-360 instrument. Water contact angles were measured using a contact meter (KRUSS CAT, Germany). X-ray photoelectron spectroscopy (XPS) was executed on an AXIS UltraDLD instrument. Photocurrent, electrochemical impedance spectroscopy (EIS) and Mott–Schottky plots were tested using a CHI-760E electrochemical workstation. Electron paramagnetic resonance (EPR) was performed using a Bruker EMXPLUS spectrometer.

2.5 Photocatalytic synthesis of H_2O_2

In a typical reaction setup, 20 mg of photocatalyst powder was dispersed in 40 mL of deionized water with stirring for 30 min in the dark. The photocatalytic reaction was initiated by irradiation of a 300 W xenon lamp (400–780 nm, 350 mW cm^{-2}) in ambient air. At designated time points, a certain suspension was taken and filtrated. H_2O_2 concentration was determined using the UV-2600 spectrophotometer at 350 nm according to iodometry (details in ESI†). The apparent quantum yield (AQY) at different irradiation wavelengths was determined using:

$$\mathrm{AQY} = \frac{2 \times \text{the number of generated } H_2O_2}{\text{the number of incident photos}} \times 100\%$$

Meanwhile, the solar-to-H_2O_2 (STH) conversion efficiency was determined using:

$$\mathrm{STH} = \frac{\Delta G(H_2O_2) \times [H_2O_2] \times V}{I \times A \times t} \times 100\%$$

where $\Delta G(H_2O_2)$ is the free energy for H_2O_2 formation (117 kJ mol^{-1}), I is the light intensity (100 mW cm^{-2}) of simulated solar light, V is the volume of suspension, A is the irradiation area, and t is the reaction time.

3. Results and discussion

3.1 Photocatalytic performance on H_2O_2 evolution

The prepared $ZnIn_2S_4$/UiO-66-X photocatalysts were evaluated to catalyze H_2O_2 generation under visible light in pure water and ambient air. UiO-66-NH_2 and $ZnIn_2S_4$ have minimal H_2O_2 evolution after 2 h illumination (9 μmol L^{-1} for UiO-66-NH_2 and 23 μmol L^{-1} for $ZnIn_2S_4$, Fig. 1a), presumably due to the limited active sites and sluggish charge separation. After $ZnIn_2S_4$ *in situ* growth on UiO-66-NH_2, H_2O_2 evolution experienced a pronounced improvement for all $ZnIn_2S_4$/UiO-66-NH_2 hybrids without exception. Thereinto, the $ZnIn_2S_4$/UiO-66-NH_2 hybrid with 50 wt% of UiO-66-NH_2 performed the highest H_2O_2 evolution. Thus, this mass ratio was selected to prepare other $ZnIn_2S_4$/UiO-66-X photocatalysts, and their corresponding activities for H_2O_2 generation were displayed in Fig. 1b. The performance of Z-U is inferior. Whereas, the H_2O_2 yields catalyzed by Z-UN, Z-U(OH)$_2$ and Z-UOH are 799, 733 and 165 μmol L^{-1}, which are 9.5, 8.7 and 2.0-fold enhancements compared with that of Z-U, respectively, affirming that the functionalization of UiO-66 by amino or hydroxyl groups could switch on the efficient photocatalytic generation of H_2O_2. Generally, the addition of sacrificial agents like alcohols and extra O_2 input are two prerequisites for efficient and continuous H_2O_2 generation by photocatalysis, yet is going against the green-chemistry principles. Comparatively, the H_2O_2 yield using Z-UN in pure water and ambient air can be even preferable to those of most MOF-based photocatalysts reacting with sacrificial agents and extra O_2 input (Table S1†), and Z-UN possesses favorable cycling performance (Fig. S1†). To study the effect of H_2O_2 decomposition, decomposition experiments with an initial H_2O_2 concentration of 1000 μmol L^{-1} were conducted over $ZnIn_2S_4$ and Z-UN (Fig. S2†). The H_2O_2 decomposition rate is greater than the generation rate after 0.5 h illumination over $ZnIn_2S_4$. While for Z-UN, the generation rate is greater than the decomposition rate until 1.5 h illumination and close to the decomposition rate after 1.5 h illumination, demonstrating that the combination with MOFs promotes the H_2O_2 formation apparently.

For comparison, 10 vol% ethanol was utilized to replace deionized water as a solution for photocatalytic H_2O_2 evolution (Fig. S3†), and the yield was boosted to 918 μmol L^{-1} using Z-UN on account of the introduction of sacrificial agents. Of note, the H_2O_2 yields using tap water and Xuanwu Lake (Nanjing, China) water can be comparable to that of using deionized water (Fig. S3†), which further improves the economy and sustainability. Meanwhile, reactions in O_2 and N_2 were also conducted using Z-UN (Fig. 1c). By comparison, O_2 promoted the H_2O_2 generation while N_2 dramatically inhibited it, shedding light on that H_2O_2 photocatalytic generation stems mainly from O_2 reduction. H_2O_2 evolution in air is close to that in O_2, implying that enough O_2 in air was adsorbed and attached on Z-UN. The AQYs of photocatalytic H_2O_2 evolution using Z-UN at wavelengths of 360, 400, 420 and 550 nm in pure water and ambient air are 1.79, 1.67, 1.3 and 0.15, respectively, which is in accord with the UV-vis DRS trend of Z-UN (Fig. 1d), indicating good light utilization. Additionally, H_2O_2 generation can still reach 717 μmol L^{-1} under simulated solar light (light filter: AM1.5, light intensity: 100 mW cm^{-1}, Fig. S4†), and the corresponding STH is calculated as 0.024%.

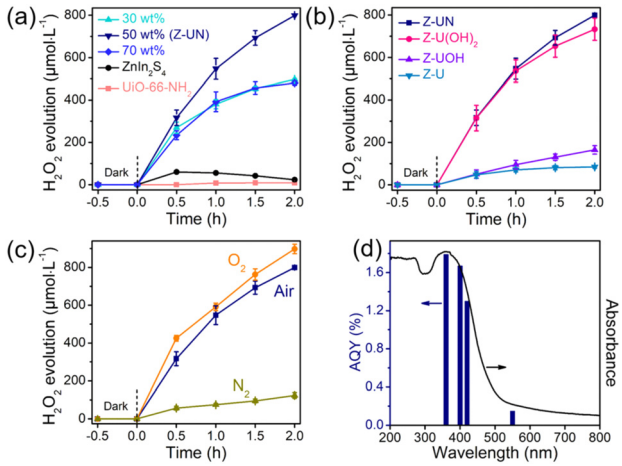

Fig. 1 Photocatalytic H_2O_2 evolution over $ZnIn_2S_4$, UiO-66-NH_2 and $ZnIn_2S_4$/UiO-66-NH_2 hybrids with 30, 50, 70 wt% of UiO-66-NH_2 (a), Z-U, Z-UOH, Z-U(OH)$_2$ and Z-UN (b), photocatalytic H_2O_2 evolution over Z-UN in O_2, air and N_2 (c), AQYs of photocatalytic H_2O_2 evolution using Z-UN at different wavelengths and UV-vis DRS of Z-UN (d). Reaction conditions: 20 mg photocatalysts, 40 mL deionized water, 400–780 nm illumination for (a)–(c), ambient air for (a), (b) and (d), ambient temperature.

3.2 Structure characterizations of the prepared $ZnIn_2S_4$/UiO-66-X

The preparation processes of the $ZnIn_2S_4$/UiO-66-X hybrids were displayed in Fig. 2a, and the only difference in these processes is the organic ligands of UiO-66-X. The XRD pattern of $ZnIn_2S_4$ has four characteristic peaks at 21.7, 27.5, 30.3 and 47.1°, ascribing to the (006), (102), (104) and (110) crystal planes of hexagonal $ZnIn_2S_4$ (Fig. 2b).[29] All functionalized UiO-66 has similar characteristic peaks compared with those of UiO-66, indicating that they are topologically equivalent to

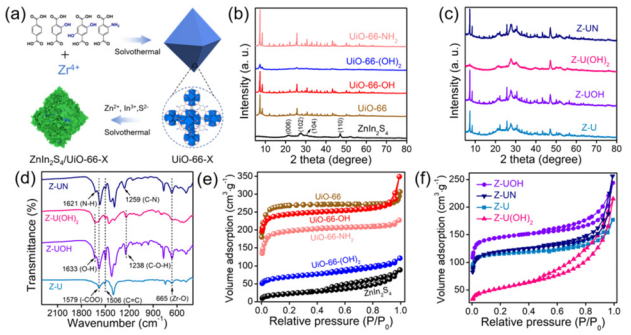

Fig. 2 Preparation diagram of $ZnIn_2S_4$/UiO-66-X hybrids (a), XRD patterns (b and c) and N_2 adsorption–desorption isotherms (e and f) of UiO-66-NH_2, UiO-66-$(OH)_2$, UiO-66-OH, UiO-66, $ZnIn_2S_4$, Z-UN, Z-U$(OH)_2$, Z-UOH and Z-U, FTIR spectra of Z-UN, Z-U$(OH)_2$, Z-UOH and Z-U (d).

the face-centered cubic lattice of the UiO-66 structure and this result is in line with the previous reports.[30,31] Evidently, the peaks attributed to $ZnIn_2S_4$ and UiO-66-X appeared on each pattern of the $ZnIn_2S_4$/UiO-66-X composites, demonstrating their successful integrations (Fig. 2c and S5†). The weak XRD peaks of UiO-66-$(OH)_2$ are triggered by its low crystallinity. In addition, the good stability of Z-UN before and after photocatalytic H_2O_2 evolution was also verified by XRD (Fig. S6†). The functional groups were identified by FTIR, and the vibration bands between UiO-66-X and the corresponding $ZnIn_2S_4$/UiO-66-X are similar (Fig. S7, S8† and 2d). All hybrids show the common bands at 1579, 1506 and 665 cm^{-1}, which are initiated by the vibrations of carboxylate groups from the terephthalic ligand, C=C bonds from the benzene ring and Zr–O bonds from Zr_6 clusters, respectively.[24] Two bands at 1621 and 1259 cm^{-1} in the spectrum of Z-UN separately correspond to the N–H bending vibration and C–N stretching vibration, demonstrating the presence of amino groups.[32] In the case of Z-U$(OH)_2$ and Z-UOH, the ν(O–H) bands and C–O stretching of hydroxyl on the benzene rings could be found at 1633 and 1238 cm^{-1}.[33] The XRD and FTIR results collectively validate the successful preparation of functionalized UiO-66 decorated by $ZnIn_2S_4$. It is known that the hydroxyl and amino functionalization would enhance the hydrophilicity. To determine this, water contact angles of Z-U, Z-UOH, Z-U$(OH)_2$ and Z-UN were measured (Fig. S9†). All samples performed good hydrophilicity because of plenty of hydroxyl groups in the metal cluster ($Zr_6O_4(OH)_4$) of Zr-MOFs. Even so, the hydroxyl and amino functionalization could still improve the hydrophilicity to a certain degree, especially for Z-U$(OH)_2$. The reinforced hydrophilicity is conducive to the H_2O_2 generation in water.

MOFs are known for their large surface area and high porosity,[34] which are advantageous for mass transfer, O_2 adsorption and attachment. The BET surface areas of UiO-66, UiO-66-OH, UiO-66-NH_2 and UiO-66-$(OH)_2$ were determined as 928, 745, 587 and 221 $m^2\ g^{-1}$, respectively (Fig. 2e). In contrast with UiO-66-X, $ZnIn_2S_4$ possesses a small surface area of 81 $m^2\ g^{-1}$. When $ZnIn_2S_4$ integrates with UiO-66-X, the surface areas could achieve noticeable magnifications to 352, 448, 361 and 178 $m^2\ g^{-1}$ for Z-U, Z-UOH, Z-UN and Z-U$(OH)_2$, respectively (Fig. 2f).

The effect of UiO-66 functionalization on the microstructure was observed by SEM. First of all, $ZnIn_2S_4$ is a distinct layer structure while it has a serious aggregation (Fig. 3a).[35] Under the same synthetic conditions except for the organic ligand categories, UiO-66-NH_2 (Fig. 3b), UiO-66-OH (Fig. 3c) and UiO-66 (Fig. 3d) present regular and uniform octahedrons, while UiO-66-$(OH)_2$ has a tiny nanoparticle morphology caused by the low crystallinity (Fig. 3e).[24] In addition, the particle sizes follow a sequence of UiO-66-$(OH)_2$ (~40 nm) < UiO-66-NH_2 (~450 nm) < UiO-66-OH (~650 nm) < UiO-66 (~950 nm), which probably induced by the steric-hindrance effect of functional groups during the crystal nucleus growth. As to Z-UN (Fig. 3f), Z-UOH (Fig. 3g) and Z-U (Fig. 3h), the corresponding UiO-66-NH_2, UiO-66-OH and UiO-66 octahedrons were evenly wrapped by $ZnIn_2S_4$ nanosheets. Conversely, for Z-U$(OH)_2$, UiO-66-$(OH)_2$ nanoparticles were loaded on $ZnIn_2S_4$ layers (Fig. 3i). Besides, the growth of $ZnIn_2S_4$ nanosheets on UiO-66-NH_2 could be tuned (Fig. S10†) and the morphology of Z-UN relatively remained unchanged after the photocatalytic H_2O_2 generation (Fig. S11†).

To further characterize the microstructure of Z-UN, TEM images of UiO-66-NH_2, $ZnIn_2S_4$ and Z-UN were conducted. The regular octahedron of UiO-66-NH_2 (Fig. 4a) and ultra-thin layers of $ZnIn_2S_4$ (Fig. 4b) could be indubitably reflected. What's more, their spatial distribution and interface contact in Z-UN can be clearly observed (Fig. 4c and d). The lattice fringe of 0.295 nm corresponding to the $ZnIn_2S_4$ (104) crystal plane in high-resolution TEM of Z-UN further validates the outer layer of $ZnIn_2S_4$ (Fig. 4d). Likewise, the (110), (104) and (102) crystal planes of $ZnIn_2S_4$ could be also indicated by the diffraction

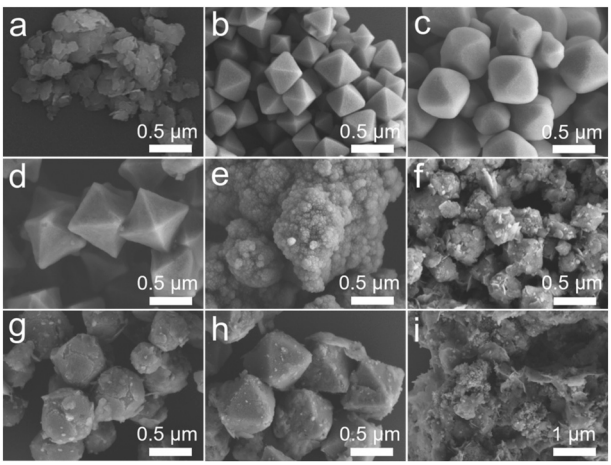

Fig. 3 SEM images of $ZnIn_2S_4$ (a) UiO-66-NH_2 (b), UiO-66-OH (c), UiO-66 (d), UiO-66-$(OH)_2$ (e), Z-UN (f), Z-UOH (g), Z-U (h) and Z-U$(OH)_2$ (i).

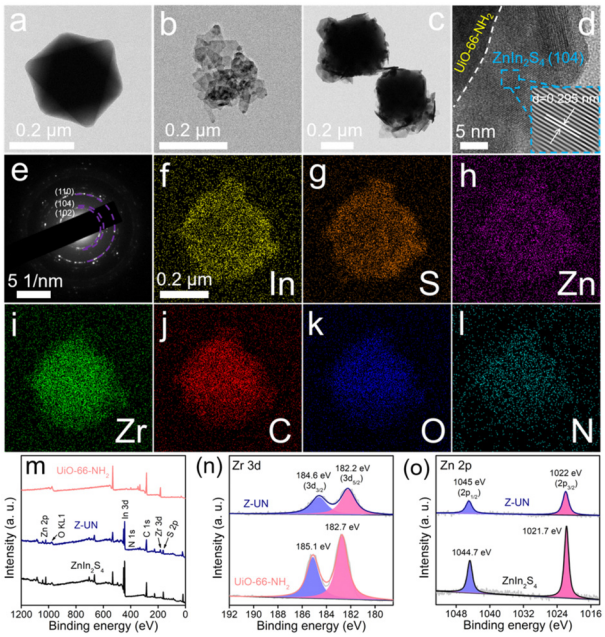

Fig. 4 TEM images of UiO-66-NH_2 (a), $ZnIn_2S_4$ (b) and Z-UN (c and d), SAED pattern (e) and EDS mapping images (f–l) of Z-UN, XPS spectra of UiO-66-NH_2, Z-UN and $ZnIn_2S_4$: survey (m), Zr 3d (n) and Zn 2p (o).

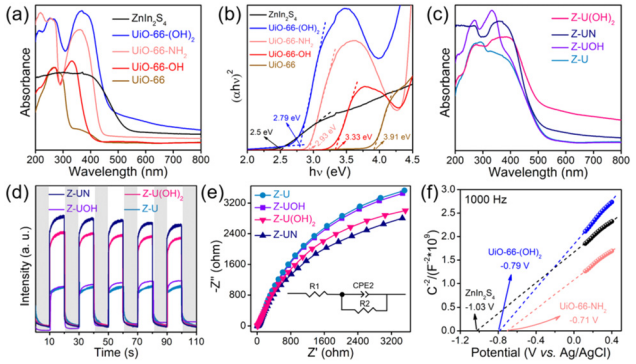

Fig. 5 UV-vis DRS (a) and $(\alpha h\nu)^2$ *versus* $h\nu$ curves (b) of $ZnIn_2S_4$, UiO-66-$(OH)_2$, UiO-66-NH_2, UiO-66-OH and UiO-66, UV-vis DRS (c), photocurrent spectra (d) and EIS Nyquist plots (e) of Z-UN, Z-U$(OH)_2$, Z-UOH and Z-U, Mott–Schottky plots of $ZnIn_2S_4$, UiO-66-$(OH)_2$ and UiO-66-NH_2 (f).

fringes of selected area electron diffraction (SAED) patterns (Fig. 4e). EDS mapping images of Z-UN uncover the uniform distribution of In, S, Zn, Zr, C, O and N elements (Fig. 4f–l), and such results indicate the formation of homogeneous interfacial junctions between $ZnIn_2S_4$ nanosheets and UiO-66-NH_2 octahedrons.

The elemental composition of In, S, Zn, Zr, C, O and N for Z-UN was further reflected by the XPS survey spectrum (Fig. 4m). The Zr 3d curve of UiO-66-NH_2 can be split into two peaks at 182.7 and 185.1 eV (Fig. 4n), which are assigned to Zr $3d_{5/2}$ and $3d_{3/2}$, respectively. Nevertheless, the two related peaks of Z-UN underwent negative shifts to 182.2 and 184.6 eV, implying a net gain of electrons for Zr^{4+}. In contrast to the peak shifts of Zr^{4+}, peaks of Zn $2p_{3/2}$ and $2p_{1/2}$ experienced high-frequency shifts from 1021.7 and 1044.7 eV of $ZnIn_2S_4$ to 1022 and 1045 eV of Z-UN, respectively (Fig. 4o), suggesting an electron loss of Zn^{2+}. Based on the gleaned above results, it is inferred that the electrons moved from $ZnIn_2S_4$ to UiO-66-NH_2 with their integration, which demonstrates the successful construction of an internal electric field between $ZnIn_2S_4$ and UiO-66-NH_2.

3.3 Mechanism discussion

The functionalization of MOFs has a huge effect on their light absorption because the functional groups could serve as auxochromic and bathochromic groups in aromatic rings.[24,25] To determine this, UV-vis DRS of UiO-66-X were performed first (Fig. 5a). UiO-66 has the smallest light absorption mainly in 200–320 nm that is aroused by the ligand-to-metal charge transfer, suggesting the bonding between carboxylate oxygen and metal.[36] By comparison, the light absorption edges of all functionalized UiO-66 underwent redshifts, especially for UiO-66-NH_2 and UiO-66-$(OH)_2$ shifting to the visible-light range, which is initiated by the conjugated π electron transition from the amino or hydroxyl-auxochromic chromophores to the Zr centers.[37] Correspondingly, the bandgaps of UiO-66, UiO-66-OH, UiO-66-$(OH)_2$ and UiO-66-NH_2 are 3.91, 3.33, 2.79 and 2.93 eV, respectively, according to the curves of $(\alpha h\nu)^2$ *versus* $h\nu$ (Fig. 5b). It should be stressed that $ZnIn_2S_4$ has an outstanding visible-light absorption with a narrow bandgap of 2.5 eV, and all $ZnIn_2S_4$/UiO-66-X heterostructures exhibit striking visible-light absorption with edges about 500 nm similar to that of $ZnIn_2S_4$ (Fig. 5c and S12†).

With the aim to validate the charge separation and transfer over $ZnIn_2S_4$/UiO-66-X heterostructures, the photocurrent and EIS were tested. At first, in comparison with $ZnIn_2S_4$ and UiO-66-NH_2, Z-UN performed with a stronger photocurrent signal and smaller arc radius of the EIS Nyquist plot (Fig. S13 and S14†), which signifies the reinforced separation of photo-excited charge carriers and diminished resistance of charge transfer. In the case of $ZnIn_2S_4$/UiO-66-X heterostructures, Z-UN and Z-U$(OH)_2$ possess more efficient charge separation and lower resistance of charge transportation than those of Z-UOH and Z-U counterparts (Fig. 5d and e), which accord well with the corresponding results of photocatalytic H_2O_2 generation. The charge transfer routes meet the thermodynamic requirements, thus the band configurations of $ZnIn_2S_4$, UiO-66-$(OH)_2$ and UiO-66-NH_2 are indispensable to be uncovered. To this end, Mott–Schottky plots of $ZnIn_2S_4$, UiO-66-$(OH)_2$ and UiO-66-NH_2 were monitored at 1000 and 2000 Hz (Fig. 5f and S15†). The flat-band potentials are −1.03, −0.79 and −0.71 V *vs.* Ag/AgCl (−0.833, −0.593, −0.513 V *vs.* NHE, $E_{NHE} = E_{Ag/AgCl} + 0.197$ V) for $ZnIn_2S_4$, UiO-66-$(OH)_2$ and UiO-66-NH_2, respectively. It is regarded that the conduction band (CB) or lowest unoccupied molecular orbital (LUMO) potentials for n-type semiconductors are more negative by 0.1 V than their flat-band potentials.[38] As such, the CB potential of $ZnIn_2S_4$,

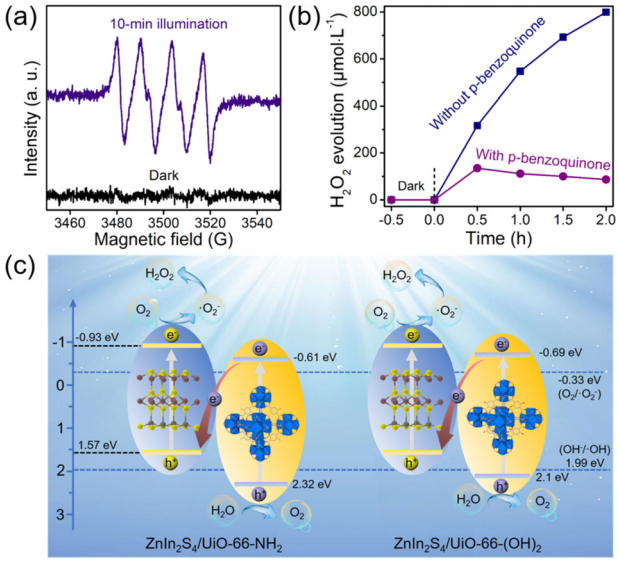

Fig. 6 EPR spectra of DMPO–$^{\cdot}O_2^-$ adducts using Z-UN at dark and 10 min illumination (a), photocatalytic H_2O_2 evolution using Z-UN with and without *p*-benzoquinone (b), the proposed mechanism for photocatalytic H_2O_2 evolution using Z-UN and Z-U$(OH)_2$ (c).

LUMO potentials of UiO-66-$(OH)_2$ and UiO-66-NH_2 are about −0.93, −0.69 and −0.61 eV, corresponding to the VB or highest occupied molecular orbital (HOMO) potentials of 1.57, 2.1 and 2.32 eV, respectively ($E_{VB\ or\ HOMO} = E_{Bandgap} + E_{CB\ or\ LUMO}$).

Although the related band configurations were known, the routes of photocatalytic H_2O_2 generation must be confirmed before elucidating the whole mechanism. Generally, it is deemed that the photocatalytic O_2 reduction into H_2O_2 experiences a direct ($O_2 + 2H^+ + 2e^- \rightarrow H_2O_2$) or indirect ($O_2 + e^- \rightarrow {}^{\cdot}O_2^-$, ${}^{\cdot}O_2^- + e^- + 2H^+ \rightarrow H_2O_2$) way.[2,20] To unveil this, the generation of $^{\cdot}O_2^-$ under visible-light illumination using Z-UN was first evidenced by EPR (Fig. 6a). Subsequently, *p*-benzoquinone was employed as a scavenger of $^{\cdot}O_2^-$ in the H_2O_2 evolution process using Z-UN. As illustrated in Fig. 6b, it is noticeable that the H_2O_2 yield has a stark decrease in the presence of *p*-benzoquinone, affirming that $^{\cdot}O_2^-$ serves as a significant intermediate species for H_2O_2 generation. Likewise, the same trend also happened on Z-U$(OH)_2$ (Fig. S16†). These results collectively suggest that photocatalytic H_2O_2 generation using Z-UN and Z-U$(OH)_2$ underwent an indirect O_2 reduction reaction.

At last, the proposed mechanism for photocatalytic H_2O_2 evolution using $ZnIn_2S_4$/UiO-66-X was discussed based on the above analyses. By means of the narrow bandgaps, $ZnIn_2S_4$ (2.5 eV), UiO-66-NH_2 (2.93 eV) and UiO-66-$(OH)_2$ (2.79 eV) are capable to be excited to generate electrons and holes by visible-light illumination (Fig. 6c). At this time, according to the band configuration of each monomer, the transfer routes of charge carriers should be determined using Z-UN and Z-U$(OH)_2$, namely, conforming to type-II or Z-scheme heterostructure. To this end, $^{\cdot}OH$ generation was tested since the corresponding potential ($E(OH^-/{}^{\cdot}OH)$ = 1.99 eV (ref. 39)) is in between the VB potential of $ZnIn_2S_4$ (1.57 eV) and HOMO potential of UiO-66-NH_2 (2.32 eV) or UiO-66-$(OH)_2$ (2.1 eV). As a consequence, $^{\cdot}OH$ generation was demonstrated by EPR spectra using Z-UN (Fig. S17†) and Z-U$(OH)_2$ (Fig. S18†), suggesting that the holes on the HOMO of UiO-66-NH_2 and UiO-66-$(OH)_2$ were kept. Thereby, Z-scheme heterostructures were formed in Z-UN and Z-U$(OH)_2$. While for Z-U and Z-UOH, the electrons would transfer from the CB of $ZnIn_2S_4$ to LUMO of UiO-66 or UiO-66-OH (Fig. S19†) because of no generation of electrons and holes by UiO-66 and UiO-66-OH. Ultimately, electrons on the CB of $ZnIn_2S_4$ in Z-UN and Z-U$(OH)_2$ possess sufficient abilities to reduce O_2 into $^{\cdot}O_2^-$ ($E(O_2/{}^{\cdot}O_2^-)$ = −0.33 eV) and further evolve into H_2O_2. Appreciably, the conspicuous visible-light absorption and unique Z-scheme heterostructures decide the superiority of Z-UN and Z-U$(OH)_2$ on photocatalytic H_2O_2 evolution in comparison with those of Z-U and Z-UOH. That is to say, the functionalization of UiO-66 does enable the efficient photocatalytic generation of H_2O_2.

4. Conclusions

To sum up, various $ZnIn_2S_4$/UiO-66-X heterostructures were fabricated for photocatalytic H_2O_2 generation under visible light in pure water. The H_2O_2 yields using $ZnIn_2S_4$/UiO-66-NH_2, $ZnIn_2S_4$/UiO-66-$(OH)_2$ and $ZnIn_2S_4$/UiO-66-OH are 799, 733 and 165 μmol L^{-1}, respectively, while the corresponding yield using $ZnIn_2S_4$/UiO-66 is only 84 μmol L^{-1}. The outstanding performances by using $ZnIn_2S_4$/UiO-66-NH_2 and $ZnIn_2S_4$/UiO-66-$(OH)_2$ are attributed to the favorable visible-light absorption and Z-scheme heterostructures. Furthermore, it is concluded that the H_2O_2 generation using $ZnIn_2S_4$/UiO-66-NH_2 and $ZnIn_2S_4$/UiO-66-$(OH)_2$ followed indirect O_2 reduction with $^{\cdot}O_2^-$ as the intermediate species. This study could provide new insight into MOF functionalization and a new doorway to green energy conversion by (photo)catalysis.

Author contributions

JQ: conceptualization, investigation, funding acquisition, and writing – original draft; LZ: data curation, formal analysis, investigation, and writing – original draft; GX, DD, YT: investigation; JY: conceptualization, resources, funding acquisition, and writing – review & editing.

Conflicts of interest

There are no conflicts of interest.

Acknowledgements

The authors are grateful for the financial supports of the Natural Science Foundation of Jiangsu Province Youth Fund (BK20210628) and the Scientific Research Foundation from Nanjing Forestry University. We also thank the Advanced Analysis & Testing Center, Nanjing Forestry

University for sample tests. JQ and LZ contributed equally to this work.

References

1 Y. Xue, Y. Wang, Z. Pan and K. Sayama, *Angew. Chem., Int. Ed.*, 2021, **60**, 10469–10480.
2 A. Gopakumar, P. Ren, J. Chen, B. V. Manzolli Rodrigues, H. Y. Vincent Ching, A. Jaworski, S. V. Doorslaer, A. Rokicińska, P. Kuśtrowski, G. Barcaro, S. Monti, A. Slabon and S. Das, *J. Am. Chem. Soc.*, 2022, **144**, 2603–2613.
3 T. Liu, Z. Pan, J. J. M. Vequizo, K. Kato, B. Wu, A. Yamakata, K. Katayama, B. Chen, C. Chu and K. Domen, *Nat. Commun.*, 2022, **13**, 1034.
4 J. Hu, T. Yang, J. Chen, X. Yang, J. Qu and Y. Cai, *Chem. Eng. J.*, 2022, **430**, 133039.
5 X. Chen, Y. Kondo, S. Li, Y. Kuwahara, K. Mori, D. Zhang, C. Louis and H. Yamashita, *J. Mater. Chem. A*, 2021, **9**, 26371–26380.
6 X. Zeng, Y. Liu, X. Hu and X. Zhang, *Green Chem.*, 2021, **23**, 1466–1494.
7 H.-I. Kim, O. S. Kwon, S. Kim, W. Choi and J.-H. Kim, *Energy Environ. Sci.*, 2016, **9**, 1063–1073.
8 L. Chen, C. Chen, Z. Yang, S. Li, C. Chu and B. Chen, *Adv. Funct. Mater.*, 2021, **31**, 2105731.
9 C. Chen, G. Qiu, T. Wang, Z. Zheng, M. Huang and B. Li, *J. Colloid Interface Sci.*, 2021, **592**, 1–12.
10 J. Qiu, X. Zhang, Y. Feng, X. Zhang, H. Wang and J. Yao, *Appl. Catal., B*, 2018, **231**, 317–342.
11 A. S. Belousov and E. V. Suleimanov, *Green Chem.*, 2021, **23**, 6172–6204.
12 J. Qiu, X.-F. Zhang, X. Zhang, Y. Feng, Y. Li, L. Yang, H. Lu and J. Yao, *J. Hazard. Mater.*, 2018, **349**, 234–241.
13 L.-Y. Wu, Y.-F. Mu, X.-X. Guo, W. Zhang, Z.-M. Zhang, M. Zhang and T.-B. Lu, *Angew. Chem., Int. Ed.*, 2019, **58**, 9491–9495.
14 H. Huang, X.-S. Wang, D. Philo, F. Ichihara, H. Song, Y. Li, D. Li, T. Qiu, S. Wang and J. Ye, *Appl. Catal., B*, 2020, **267**, 118686.
15 Y. Kondo, Y. Kuwahara, K. Mori and H. Yamashita, *Chem*, 2022, **8**, 2924–2938.
16 Y. Isaka, Y. Kawase, Y. Kuwahara, K. Mori and H. Yamashita, *Angew. Chem., Int. Ed.*, 2019, **58**, 5402–5406.
17 Y. Kawase, Y. Isaka, Y. Kuwahara, K. Mori and H. Yamashita, *Chem. Commun.*, 2019, **55**, 6743–6746.
18 Y. Wu, X. Li, Q. Yang, D. Wang, F. Yao, J. Cao, Z. Chen, X. Huang, Y. Yang and X. Li, *Chem. Eng. J.*, 2020, **390**, 124519.
19 Y. Zhao, Y. Liu, J. Cao, H. Wang, M. Shao, H. Huang, Y. Liu and Z. Kang, *Appl. Catal., B*, 2020, **278**, 119289.
20 C. Liu, T. Bao, L. Yuan, C. Zhang, J. Wang, J. Wan and C. Yu, *Adv. Funct. Mater.*, 2022, **32**, 2111404.
21 H. Jasuja, G. W. Peterson, J. B. Decoste, M. A. Browe and K. S. Walton, *Chem. Eng. Sci.*, 2015, **124**, 118–124.
22 A. Jrad, M. Hmadeh, G. Awada, R. Chakleh and M. Ahmad, *Chem. Eng. J.*, 2021, **410**, 128237.
23 D. Chen, W. Yang, L. Jiao, L. Li, S.-H. Yu and H.-L. Jiang, *Adv. Mater.*, 2020, **32**, 2000041.
24 Y. L. Wang, S. Zhang, Y. F. Zhao, J. Bedia, J. J. Rodriguez and C. Belver, *J. Environ. Eng.*, 2021, **9**, 106087.
25 H. Liu, M. Cheng, Y. Liu, G. Zhang, L. Li, L. Du, B. Li, S. Xiao, G. Wang and X. Yang, *Coord. Chem. Rev.*, 2022, **458**, 214428.
26 J. Qiu, Y. Feng, X. Zhang, M. Jia and J. Yao, *J. Colloid Interface Sci.*, 2017, **499**, 151–158.
27 J. Qiu, L. Zhang, D. Dai, G. Xia and J. Yao, *ChemSusChem*, 2022, **15**, e202200399.
28 H. Su, C. Rao, L. Zhou, Y. Pang, H. Lou, D. Yang and X. Qiu, *Green Chem.*, 2022, **24**, 2027–2035.
29 Y. Qin, H. Li, J. Lu, Y. Feng, F. Meng, C. Ma, Y. Yan and M. Meng, *Appl. Catal., B*, 2020, **277**, 119254.
30 S. Li, S. Sun, H. Wu, C. Wei and Y. Hu, *Catal. Sci. Technol.*, 2018, **8**, 1696–1703.
31 Y. Sun, M. Chen, H. Liu, Y. Zhu, D. Wang and M. Yan, *Appl. Surf. Sci.*, 2020, **525**, 146614.
32 G. W. Peterson, J. J. Mahle, J. B. DeCoste, W. O. Gordon and J. A. Rossin, *Angew. Chem.*, 2016, **128**, 6343–6346.
33 J. Liu, X. Huang, L. Liu, Q. Nie, Z. Tan and H. Yu, *J. Environ. Eng.*, 2022, **10**, 108294.
34 Y. Li, F. Ma, L. Zheng, Y. Liu, Z. Wang, P. Wang, Z. Zheng, H. Cheng, Y. Dai and B. Huang, *Mater. Horiz.*, 2021, **8**, 2842–2850.
35 C. Du, Q. Zhang, Z. Lin, B. Yan, C. Xia and G. Yang, *Appl. Catal., B*, 2019, **248**, 193–201.
36 R. W. Liang, F. F. Jing, L. J. Shen, N. Qin and L. Wu, *J. Hazard. Mater.*, 2015, **287**, 364–372.
37 X. Mu, J. Jiang, F. Chao, Y. Lou and J. Chen, *Dalton Trans.*, 2018, **47**, 1895–1902.
38 J. Qiu, D. Dai, L. Zhang, G. Xia and J. Yao, *Sep. Purif. Technol.*, 2022, **301**, 121990.
39 J. J. Shi, S. D. Li, F. M. Wang, Y. M. Li, L. N. Gao, X. R. Zhang and J. Lu, *Catal. Sci. Technol.*, 2018, **8**, 6458–6467.